Vacuum 174 (2020) 109183

Contents lists available at ScienceDirect

Vacuum

journal homepage: http://www.elsevier.com/locate/vacuum

Radiation-induced swelling and hardening of 316L stainless steel fabricated by selected laser melting

Jiwei Lin [a], Feida Chen [a], Xiaobin Tang [a,b,*], Jian Liu [a], Shangkun Shen [a], Guojia Ge [a]

[a] Department of Nuclear Science & Technology, Nanjing University of Aeronautics and Astronautics, Nanjing, 211106, China
[b] Key Laboratory of Nuclear Technology Application and Radiation Protection in Astronautics (Nanjing University of Aeronautics and Astronautics), Ministry of Industry and Information Technology, Nanjing, 211106, China

ARTICLE INFO

Keywords:
Selective laser melting
Stainless steel
Phase transformation
Swelling
Radiation hardening

ABSTRACT

Additive manufacturing (AM) has remarkable application potential in the field of nuclear engineering materials. Although considerable effort has been exerted to improve the mechanical properties of additive-manufactured materials, research on radiation-induced degradation of AM materials must also be conducted to meet the needs of nuclear engineering. This paper describes the radiation-phase stability of 316L stainless steel (SS) fabricated via selective laser melting (SLM) technology and the influence of microstructure change on the swelling and hardening of materials. Results showed that the austenite phase in SLM 316 SS was more stable than that of cold-rolled (CR) 316L SS. However, the swelling of SLM 316L SS occurred earlier than that of CR 316L SS in the room temperature (RT) case, while no distinct difference was observed between the two materials in the 350 °C case. Two 316L SSs behave differently in swelling, due to their difference in misorientation and density of grain boundaries and dislocations. In addition, the hardening of CR 316L SS was stronger than that of SLM 316L SS. Analysis indicates that the inhibiting effect on radiation-induced martensite formation in SLM 316L SS leads to the improved resistance to the radiation hardening.

1. Introduction

The components used in nuclear power engineering generally have complex structures and connections that require secondary thermal processing in their raw materials [1]. Given that thermal processing changes the microstructure of the material, the mechanical and corrosion properties and radiation resistance of the final formed component differ from those of raw materials. This remarkably increases the complexity and time consumption of the development and assessment of nuclear engineering materials.

Selective laser melting (SLM) [2] is an emerging additive manufacturing (AM) laser technology characterized by design freedom and short lead time in complex geometry processing. Compared with other AM methods, SLM has the advantages of high precision and excellent surface quality; hence, parts manufactured via SLM can be used directly after sandblasting or polishing with excellent mechanical properties [3] and corrosion resistance [4]. SLM technology possesses characteristic of one-step forming. Thus, it can be used not only to simplify the component development of Generation-IV nuclear power plants, but also to reduce the cost and time consumption of structural material upgrade of fuel assembly in Generation-II nuclear power plants.

316L stainless steel (SS) is widely used as a structural material for the fuel assembly of Generation-II nuclear reactors and an important candidate material for many Generation-IV reactors, such as high-temperature gas-cooled, sodium-cooled fast, lead–bismuth-cooled, and thorium-based molten salt reactors, because of its excellent performance and low price [5]. In addition, 316L SS is the most mature among additive-manufactured metal materials. Although considerable effort has been exerted to improve the mechanical properties of AM 316L SS to meet the needs of nuclear engineering [6,7], research on the changes of the microstructure and performance degradation of AM 316L SS induced by radiation must also be conducted. However, only a few studies have been conducted on the radiation damage of AM 316L SS [8–12]. Certain studies have focused on the interaction of microstructures in SLM 316L SS with radiation-induced defects and impurity atoms. The findings showed that the sub-grain boundaries (SGBs) and nano-oxides in SLM 316L SS affected the distribution of He bubbles [12], dislocation loops [10], and voids [8]. However, minimal information is available on the specific macroscopic manifestations of radiation damage in SLM 316L SS. Although SLM 316L SS exhibited good resistance to

* Corresponding author. Department of Nuclear Science & Technology, Nanjing University of Aeronautics and Astronautics, Nanjing, 211106, China.
E-mail address: tangxiaobin@nuaa.edu.cn (X. Tang).

https://doi.org/10.1016/j.vacuum.2020.109183
Received 28 October 2019; Received in revised form 5 January 2020; Accepted 7 January 2020
Available online 10 January 2020

irradiation-assisted stress corrosion cracking [11] and He-induced hardening [12], the usual manifestations of radiation effect, such as phase transition, surface swelling, and radiation defect-induced hardening remain unclear. Hence, more evidences on the performance and mechanism of radiation damage in SLM 316L SS still need to be provided.

In this work, we conducted 5 MeV Xe^{23+} beam irradiation experiments on SLM 316L SS at room temperature (RT) and 350 °C (PWR operating temperature). Previous studies have shown that the dislocation loop density of SS is saturated when the irradiation dose reaches 1 displacement per atom (dpa) [10,13]. Therefore, 0.69 and 3.7 dpa were selected in our experiment. For comparison, the same experiments were further conducted on traditional cold-rolled (CR) 316L SS. The microstructure evolution, surface swelling, and radiation hardening behavior of the two steels were characterized using grazing incidence X-ray diffraction (GIXRD), atomic force microscopy (AFM), transmission electron microscopy (TEM), and nanoindentation. The mechanism of SLM 316L SS radiation damage was analyzed in detail to evaluate its radiation resistance.

2. Material and methods

2.1. Materials

The SLM 316L SS used in this work was a rectangular parallel-piped bulk of 5 × 3 × 3 cm^3, printed in an SLM BLT-S300 facility (Xi'an Bright Laser Technologies Co., China) equipped with an IPG fiber laser with a maximum 500 W power output and 70 μm diameter laser spot. During the building process, the fixed laser parameters (200 W power, 850 mm/s scan speed, and 0.1 mm line spacing) were used to obtain the samples with the highest density. Commercial 316L SS with a size of 10 × 10 × 1 cm^3, fabricated via traditional craft, was purchased from Wuxi Xinguangda Stainless Steel Co., Ltd. Subsequently, the commercial 316L SS bulk was annealed for 2 h at 1373 K under high vacuum condition (~10^{-5} Pa) and then 15% deformed through cold rolling. Both 316L SSs were cut into small disks with size of Φ10 mm × 0.5 mm, and then mechanically polished into mirrors respectively. There were another group of SLM 316L SS TEM foils which were prepared by a standard double-jet procedure (7 vol% per-chloric acid and 93 vol% ethanol with a voltage of 65 V at −25 °C). The TEM specimens were used to explore the element segregation of SLM 316L SS and further irradiated under 3.7 dpa Ar^+ at RT. The chemical composition of the two 316L SSs is listed in Table 1.

The microstructures of both steels are shown in Fig. 1. As shown in Fig. 1(c), SLM 316L SS shows a unique layer band structure corresponding to the top side of the building bulks (perpendicular to building direction). There were numerous SGBs and nano-inclusions in SLM 316L SS. The cellular SGB structure is often aligned with the temperature gradient direction in the solidification process [14]. The elemental maps from energy dispersive spectroscopy (EDS) analysis showed that element segregation at SGBs and nano-inclusions in Fig. 3. The result showed that heavier elements (Mo, Ni) or larger elements (Cr, Mn) than Fe were enrichment at SGBs. On the contrary, Fe was depletion. Owing to extremely fast cooling rate (10^6 K/s), there is not enough time for the diffusion and alloying of atoms to be completed during rapid crystal growth. The uneven diffusion took place around SGBs. It is well documented that significant tensile residual stresses are generated upon solidification for SLM 316L SS [15]. Birnbaum [15] indicated that the strain energy field generated around SGBs would drive solute diffusion to minimize local free energy via the formation of Cottrell atmospheres, which results in stable element segregation at SGBs. The EDS elemental mapping further confirmed that the embedded nano-inclusions contain Si, Mn and O. The presence of oxide dispersions in AM austenitic SS has been previously reported [6,12]. The likely sources of oxygen are the native oxide on the powder surface and (gas) impurities in the AM process atmosphere. Although a vacuum treatment (0.1 Pa) was executed before printing, there was still residual oxygen in the chamber. Due to the strong affinity of O element with Si and Mn, the Mn and Si elements in the powder will be spontaneously adsorbed by O to form inclusions during the process of laser melting. The average size and number density of inclusions in our work were measured approximately 60 nm and 4.2 × 10^{20} m^{-3}, respectively. And the overall volume percentage of inclusions obtained was approximately 5 vol%.

Table 1
Nominal chemical compositions (wt%) of the two types of 316L SS.

	Cr	Ni	Mo	Mn	Si	C	S	P
SLM	17.17	10.45	2.22	1.20	0.52	0.017	0.014	0.031
CR	16.64	10.05	2.02	1.18	0.44	0.020	0.002	0.031

2.2. Irradiation

The as-prepared disk specimens were irradiated at RT and 350 °C with 5 MeV Xe^{23+} ions at a flux of approximately 1.139 × 10^8 ions/(cm^2·s) in a chamber with a vacuum of 10^{-5} Pa on the 320 kV platform at the Institute of Modern Physics in the Chinese Academy of Sciences. Fluence was set to 2.6 × 10^{14} and 1.4 × 10^{15} ions/cm^2. The damage profiles were calculated using SRIM-2013 software (Fig. 3) in which the displacement energy of Fe, Cr, and Ni was 40 eV and that of Mo was 60 eV. SRIM-2013 was also used to obtain the corresponding dpa values, which were calculated at 0.69 and 3.7 dpa. The results were obtained using "Kinchen–Pease quick calculation." The radiation damage depth (distribution) under 5 MeV Xe^{23+} ions was calculated at 1000 nm, wherein the peak damage occurred at 600 nm.

The implantation experiments for SLM 316L SS TEM foil was carried out on a 100 kV ion implanter in Special Equipment Safety Supervision Inspection of Jiangsu Province. The samples were irradiated by 80 keV Ar ions to achieve a fluence of 2.96 × 10^{15} ion/cm^2 (3.7 dpa) at RT. The SRIM calculation result was shown in supplementary material.

2.3. Characterization

The pre-irradiation microstructure of the SLM and CR 316L samples were characterized via OM (Zeiss Scope A1), SEM (Apollo 300), and TEM (Tecnai G2 F20 S-Twin).

Residual gas contamination (C, H, O and N) was measured by infrared absorption carbon-sulfur analyzer (LECO, CS844) and oxygen nitrogen hydrogen analyzer (LECO, ONH836). The measurement accuracy reaches 1 ppm (wt).

The GIXRD (Bruker D8 ADVANCE) measurements were conducted with a Cu K_α radiation source (λ = 1.5406 Å) to detect the phase changes in the irradiation layers. X-ray scanning ranged from 30° to 90° with a 0.02° resolution. In accordance with the penetration depth of Xe irradiation (approximately 0.6–1 μm), the incident angle of 3° was selected to detect the microstructure change in the irradiation damage region.

AFM was performed at RT using a Dimension Icon, an AFM equipment made by Bruker, to analyze the surface information of the irradiated and unirradiated regions. The AFM image was acquired using the ScanAsyst mode with a ScanAsyst air probe. The maximum scanning region was 30 × 30 $μm^2$ in this experiment.

Nanoindentation tests were performed using a diamond Berkovich indenter in a Nano Indenter G200 (Agilent Technologies) with a continuous stiffness measurement mode at the Suzhou Institute of Nano-Tech and Nano-Bionics. Hardness was calibrated to a depth of 1.5 μm using a fused silica reference material. The maximum penetration depth and applied load were approximately 1.5 μm and 500 mN, respectively. Each specimen was tested at five different points, and the distance between indentations was ~30 μm (20 times the penetration depth).

Cross-sectional specimens for TEM were extracted from the irradiated surfaces with a focused ion beam (FEI Helios Nanolab 600) using 30 kV Ga^+ ions for machining, followed by 5 kV Ga^+ ions for polishing

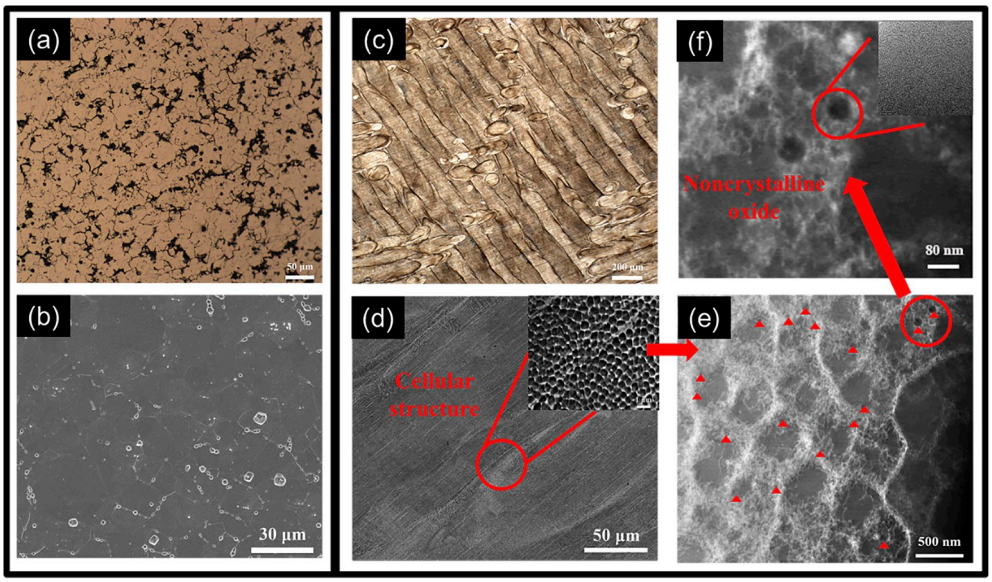

Fig. 1. Pre-irradiation microstructure of CR and SLM 316L SS: (a) Optical micrograph (OM) of martensite (black precipitate) in CR 316L SS, (b) scanning electron microscopy (SEM) of grains in CR 316L SS, (c) OM image of SLM 316L SS revealing the unique structure of the layer band in the AM material, (d) SEM of cellular subgrains in SLM 316L SS, (e) scanning TEM (STEM) image of cellular subgrains and nanoinclusions in SLM 316L SS, and (f) enlarged STEM image of nanoinclusions.

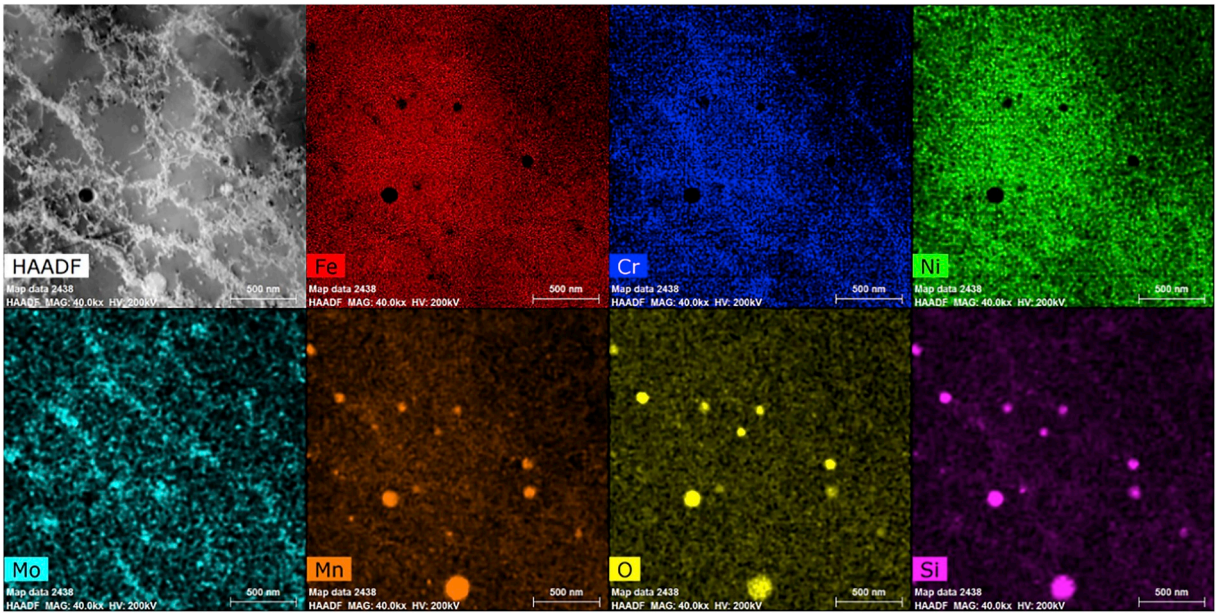

Fig. 2. STEM-EDS image of SLM 316L SS.

with a vacuum of 6.5 × 10^{-4} Pa. Conventional TEM imaging of irradiation-induced microstructural evolution was performed using a Tecnai G2 F20 S-Twin with a maximum accelerating voltage of 200 kV.

3. Results

3.1. Influence of residual gas contamination under irradiation

Molecules in air could hinder the movement of ions. To ensure the intensity and stability of the ion beam, vacuum conditions (<10^{-4} Pa) are necessary. However, trace gas remained in the chamber and may affect the composition of the samples during irradiation at high temperatures. There is about 78% N_2, 21% O_2, 0.94% inert gas, 0.03% CO_2, and 0.03% other impurities (such as O_3, H_2O, NO and NO_2 etc.) in air (proportionate by volume). Therefore, we measured the gas element composition (C, H, O and N) of SLM 316L SS before and after irradiation to 3.7 dpa at 350 °C, as shown in Table 2. It was showed little change in gas element content before and after irradiation, which proved that the vacuum condition was qualified.

3.2. GIXRD

Fig. 4 shows the GIXRD patterns of (a) SLM and (b) CR 316L SS under different irradiation conditions. SLM 316L SS maintained the single-phase austenite γ (FCC) structure without phase transition under any experiment condition, and the lattice constant was maintained at 3.6021 Å. The texture orientation changed merely from γ (111) to γ (200) at 350 °C. From the comparison, CR 316L SS originally contained some martensite α' (BCC) due to cold processing. A significant phase transition (γ (FCC) → α' (BCC)) occurred in CR 316L SS when the

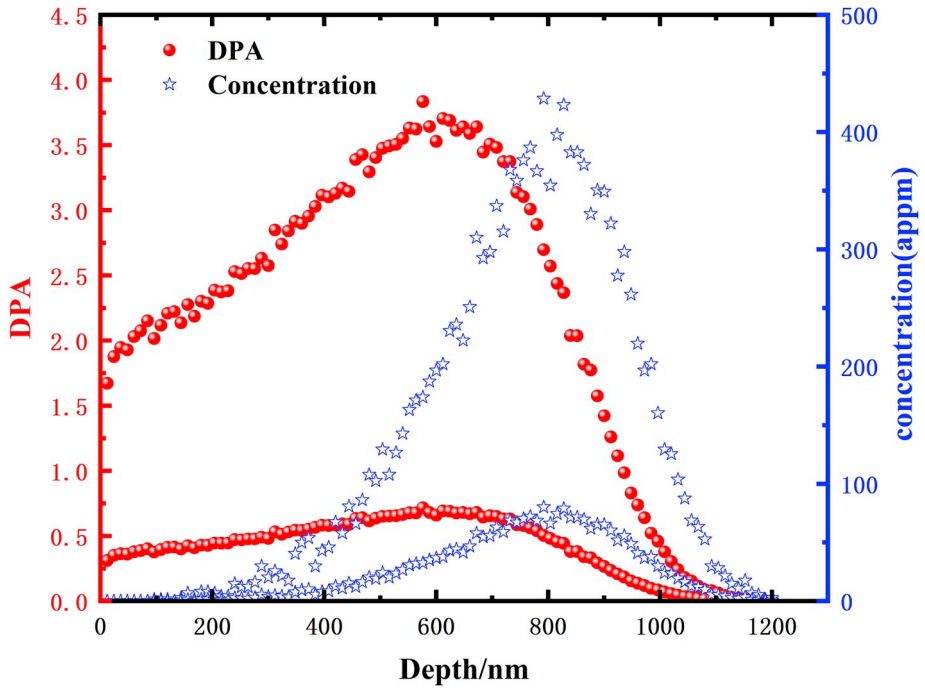

Fig. 3. Distribution of displacement damage and Xe concentration versus depth in 316L SS irradiated with 5 MeV Xe ions according to SRIM-2013.

Table 2
The composition (wt%) of SLM 316L SS before and after irradiation to 3.7 dpa at 350 °C.

	H	C	N	O
Unirradiated	<0.0001	0.017	0.099	0.035
350 °C 3.7 dpa	0.0002	0.016	0.100	0.035

irradiation dose reached 3.7 dpa. The lattice constant increased from 3.5989 Å to 3.6005 Å after irradiation.

Fig. 4(c) presents the CR 316L SS martensite content, which is calculated using the method proposed by Amar [16]. The degree of phase transition was small at 0.1% and 0.9% after a dose of 0.69 dpa at RT or 350 °C, respectively. As the ion dose increased to 3.7 dpa, the degree also increased significantly. Kumar [17] mentioned that radiation-induced phase transition is the result of defect accumulation and temperature variation. In this study, the temperature range of RT to 350 °C demonstrated a minimal effect on the radiation-induced phase transition. The phase change may be dominated by the accumulation of radiation-induced defects. Compared with its CR counterpart, SLM 316L SS presented improved phase stability under irradiation. From a mechanical point of view, grain refinement aids in radiative stress dispersion and preventing stress concentration to produce deformed martensite [18]. This mechanism can also explain the inhibition of radiation-induced phase decomposition in nanocrystalline materials. High-density subgrains may be an important factor in improving the resistance of SLM 316L SS to radiation-induced phase transition.

3.3. AFM

Fig. 5 illustrates the AFM 3D image of the irradiated area and matrix of (a) SLM and (b) CR 316L SSs at an irradiation dose of 3.7 dpa at 350 °C. The results showed that the two steels had clear surface swelling under this condition. We compared the swelling heights of the two steels, as shown in Fig. 3(e), and calculated the swelling rate (swelling height/irradiation depth (1 μm)), as shown in Table 3. No significant difference existed in the swelling rate between the two steels at ~1%. AFM testing of samples under other irradiation conditions (see Fig. S2) was also performed. No swelling was observed on the irradiated surface in the samples under other irradiation conditions, except for an approximately 0.7% swelling of SLM 316L SS after 3.7 dpa irradiation at RT. The sample surface roughness (Ra = 4–6 nm) interfered with the observation of the low swelling height.

According to our results, radiation swelling in SLM 316L SS appeared earlier than that in CR 316L SS at RT. The difference in swelling is likely due to the following reasons: First, contrary to the vacancies, the SGB structure of SLM 316L SS had a strong trapping effect on interstitials that promote swelling. Meric [8] confirmed this result. Second, the BCC structure had fewer interstitial sites for jumping compared with the FCC structure [19]. Therefore, the BCC structure exhibited strong resistance to radiation swelling. The GIXRD results showed that the BCC structure originally existed in CR 316L SS, and the BCC content increased after irradiation. Hence, SLM 316L SS is more swollen than its CR counterpart at RT. The difference in the swelling degree between the two steels decreased at 350 °C. This may be due to the decrease in the diffusion rate difference between interstitial and vacancy atoms as the temperature increased.

3.4. Nanoindentation

Fig. 6 shows the change of hardness with depth before and after irradiation of SLM and CR 316L SS. To avoid the anti-nanoindentation size effect [20], we did not analyze data with a depth less than 100 nm. The results showed that the hardness of SLM and CR 316L SS decreased with the increase in indentation depth due to the size effect of the indenter. This effect can be explained by the theoretical model of geometrically necessary dislocation proposed by Nix and Gao [21]. This model predicts the hardness measured by the nanoindenter as follows:

$$H = H_0\sqrt{1 + h^*/h}, \quad (1)$$

where H_0 is the hardness at infinite depth, h is the indentation depth of the indenter, and h^* is a characteristic length depending on the shape of the indenter tip and material type.

Fig. 6(a) and (b) show that the hardness of both irradiated 316L SS is larger than that of the unirradiated specimens. Moreover, the hardening degree of CR 316L SS was higher than that of SLM 316L SS. The

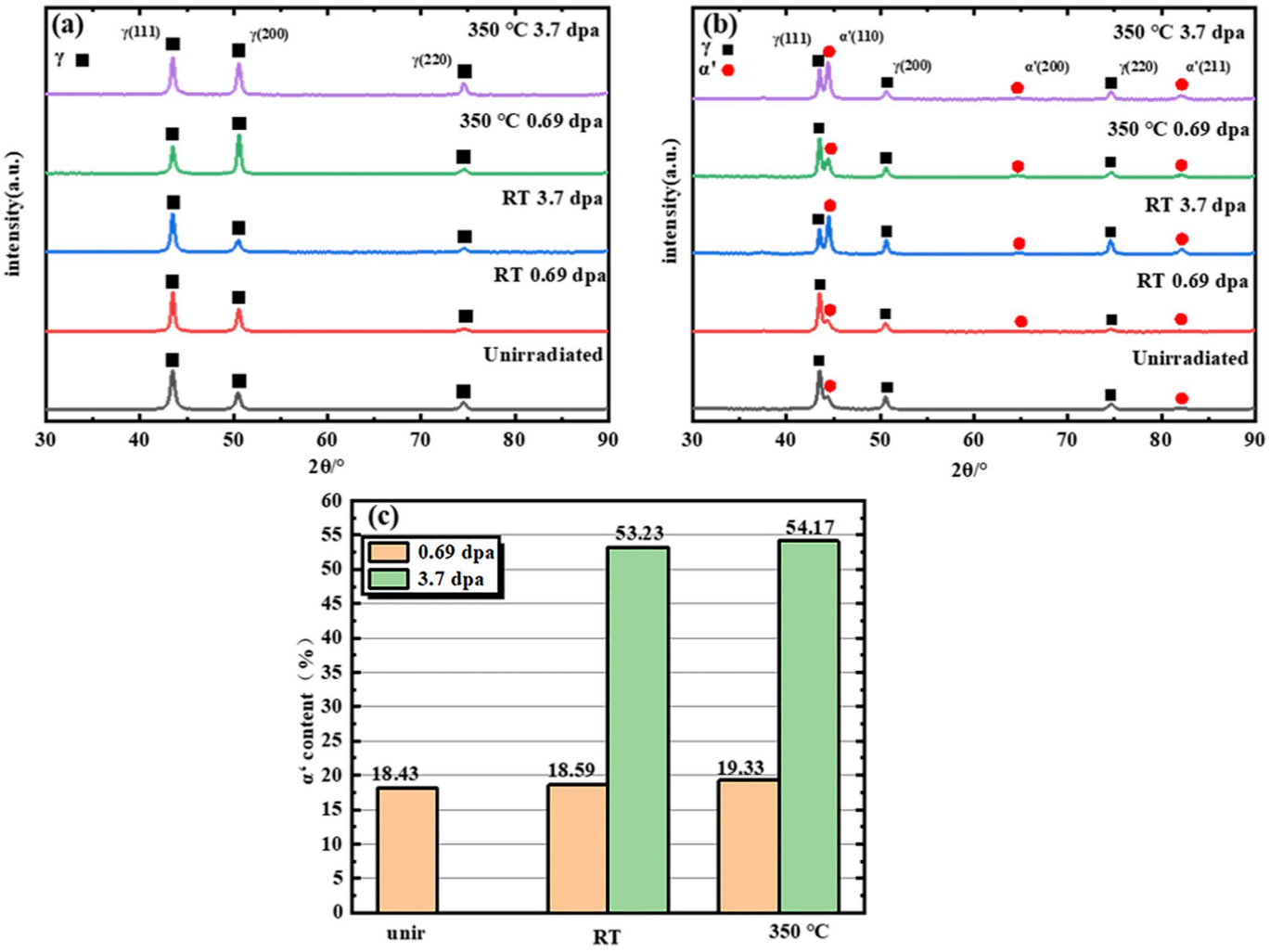

Fig. 4. GIXRD patterns of Xe irradiated with (a) SLM and (b) CR 316L SSs; (c) martensite content (%) in CR 316L SS calculated from the GIXRD results.

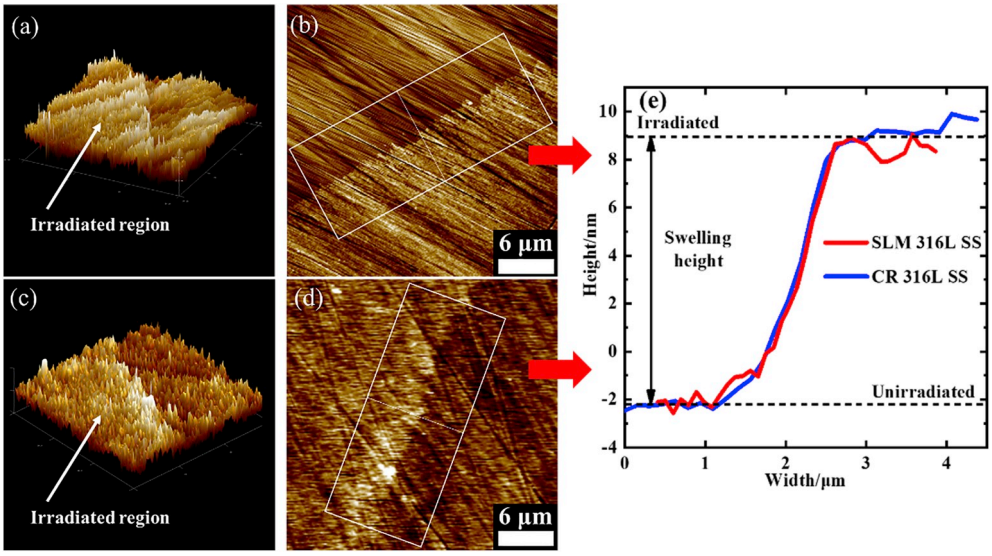

Fig. 5. AFM image of the irradiated and unirradiated regions of the (a, b) SLM and (c, d) CR at 3.7 dpa under 350 °C; (e) measured swelling heights in (b) and (d).

increasing degree of hardness for all the specimens was characterized by the ratio of H^{irr}/H^{unirr}, as shown in Fig. 6(c) and (d). The findings indicate that the critical indentation depth (h_c) was ~250 nm, which was approximately one-fourth of the thickness (~1000 nm) of the irradiation layer (as shown in Fig. 2). To obtain the true hardness of the irradiated layer, we used the method developed by Kasada [22]. We illustrated the

Table 3
Swelling rates of the irradiated SLM and CR 316L SS at 3.7 dpa.

	SLM	CR
RT 3.7 dpa	0.7%	\
350 °C 3.7 dpa	1%	1%

relation curve of H^2-1/D (as shown in Fig. 6(e) and (f)) to obtain the macroscopic hardness, H_0. In the case of unirradiated specimens, the curve demonstrated good linearity within a range of $h > 100$ nm. However, the irradiated specimens presented bilinearity and a transition depth ranging from 200 nm to 250 nm, which was consistent with h_c. Beyond h_c, the soft bulk region could contribute to the hardness value with increasing indentation depth; hence, the data in the range of 100 nm $< h <$ 250 nm were selected to calculate H_0^{IIT}, as shown in Fig. 6(g). Before irradiation, it was found the H_0 of SLM 316L SS is higher than that of CR 316L SS. The hardening of SLM alloys was related to the strengthening effect of SGB, nanoinclusions and dislocations, which can hinder dislocation motion.

Fig. 6(h) shows the relationship between the hardening fraction and irradiation dose of the two steels in this study and in the research results of Huang [23] and Hunn [13]. The results showed that hardening was enhanced with increasing irradiation dose and reached saturation at a certain point. This phenomenon could be attributed to the formation of radiation-induced defects (such as dislocation loops) and precipitated phases. These defects and precipitates acted as anchors for dislocation and resulted in hardening. The number of irradiation defects was basically saturated after reaching a certain irradiation dose, and subsequent hardening became not obvious. By comparing the radiation hardening fractions at different temperatures, we found that both steels had a greater degree of hardening at RT compared with that at 350 °C. Theiss [24] determined that the vacancies became migratory at temperatures greater than 0.17 T_m (T_m is the melting point of the material). The temperature (350 °C) of our experiment reached 0.3 T_m; hence, additional vacancies were annihilated with interstitials and reduced the number of defects, thereby weakening the hardening effect.

The results in Fig. 6 show that the hardening of SLM 316L SS is less than that of CR 316L SS. The factors contributing to hardness change, such as the formation of radiation defects and phase transition, were complex. Hardening combined with the TEM results is explained in the Discussion Section.

3.5. TEM

The overall microstructure of the two 316L SSs after an irradiation dose of 3.7 dpa is shown in Fig. 7. Fig. 7(a) presents that many twins (yellow ellipses) occur at a depth of around 1 μm (in line with the SRIM simulation results) of irradiated SLM 316L SS at RT. Moreover, many nanotwins appeared inside the material (see Fig. S4). Some studies attribute this phenomenon to the effect of radiation stress release [25,26]. However, this type of twin was absent at 350 °C (Fig. 7(b)), which was consistent with the fact that twins are unstable at high temperatures [27]. Fig. 7(c) shows the overall image of CR 316L SS irradiated at RT. Many twins, dislocations, and some martensite existed in the matrix and formed during the cold rolling process. Depending on the increasingly concentrated radiation-induced stress, dislocations could interact with twins in several configurations to cause detwinning and form martensite [28–30]. Thus, a reduced number of twins existed in the irradiated layer of CR 316L SS. A clear martensite phase could exist in CR 316L SS through electron diffraction of selected areas. This finding is consistent with that of the γ→α'Pitsch model $[001]_\gamma//[011]_{\alpha'}$ [31], as shown in Fig. 7(c) and (d). Surprisingly, a recrystallized layer was also observed in the irradiated region. The specific reason for the formation of a recrystallized layer remains unclear, but it is likely due to the excessive surface temperature caused by the high radiation dose rate.

During the rapid cooling process, the supersaturated thermal equilibrium vacancies agglomerate and collapse, forming dislocation loops in materials. Such loops are commonly known as quenched vacancy dislocation loops [32]. In FCC metal such as aluminum [32] and austenitic stainless steel [33], quenched vacancy loops nucleate on (110) planes with Burgers vectors of ±a/2 [011]. Cooling rates for materials fabricated by SLM is about 10^6 K/s. Therefore, the formation of vacancy loops in SLM 316L is not surprising. As shown in Fig. 8, the dislocation loops broadened at g = 200 (pattern a), and shrink at g = −200 (pattern b). The Burgers vector b of the dislocation loop was determined in accordance with the invisibility criterion at a/2<110>. Dislocation loops are further identified as vacancy loops by the inside-outside approach (b·z > 0, z is the incident direction of the electron beam). The number densities and the size of vacancy loops in SLM 316L SS as estimated at approximately 20.8 nm and 2.8 × 10^{20} m^{-3}, which were close to the result of size in Kaplanskii et al. [34]. (10–25 nm for SLM NiAl based alloy).

Unlike quenched vacancy loops, dislocation loops produced by austenitic stainless steel under ion irradiation are generally interstitial type [10,23]. As shown in Fig. 9, most of the dislocation loops shrink at g = 200 (pattern a and c), and broadened at g = −200 (pattern b and d), which is contrary to the results of Fig. 8. The crystal belt axis orientation we observed was B = [011], and the Burgers vector *b* of the dislocation loop was determined in accordance with the invisibility criterion at a/2<110> and a/3<111> for the perfect and faulted, respectively. Given that b·z < 0, the dislocation loops were considered to be an interstitial type [35]. The number density and the average size of interstitial loops at RT and 350 °C of SLM 316L SS were 4.7 × 10^{21} $m^{-3}$and 6.4 nm, and 1.9 × 10^{22} $m^{-3}$and 6.4 nm, respectively. Irradiation-induced interstitial dislocation loops are smaller in size and higher in number density than quenched vacancy loops in SLM 316L SS. Kiritani [32] observed similar phenomenon in quenched aluminum after irradiation.

Fig. 10 includes the microscopic images of radiation-induced defects containing the dislocation loops, dislocation lines, and certain dark spots. Small α′ phase generations were also observed in CR 316L SS. The statistical results of the dislocation loop size are shown in Fig. 10(e) and (f) (The dislocation lines were not counted because determining whether they were generated by irradiation is difficult). The number density of irradiation-induced interstitial dislocation loops was an order of magnitude greater than that of quench induced vacancy loops in SLM 316L SS. Moreover, Kiritani [32] indicated quench induced vacancy loops would shrink and disappear by irradiation owing to the absorption of interstitial atoms. In particular, the vacancy loops are unstable under irradiation above 300 °C [36], and the number density will decrease due to the thermal emission of the vacancy. Therefore, the pre-existing vacancy loops did not interfere with our statistics of the irradiation-induced dislocation loops at RT and 350 °C. The results showed that the average size of the dislocation loop of CR and SLM 316L SS at RT was ~6.4 and ~6.8 nm, which were close to the results in Huang [23] (~7 nm for irradiated CW 316 SS, 3.7 dpa, RT). At 350 °C, the average size of the dislocation loop of CR 316L SS tended to increase, whereas the average size of SLM 316L SS did not change significantly. However, regardless of RT or 350 °C conditions, the average loop size of SLM 316L SS was smaller than that of CR 316L SS. The number densities and the dislocation loop size of SLM and CR 316L SS were estimated at approximately 4.7 × 10^{21} and 1.5 × 10^{21} m^{-3} at RT and 1.9 × 10^{22} and 2.5 × 10^{21} m^{-3} at 350 °C, respectively. These results were consistent with the previous results for irradiated 316L SS, which demonstrated loop number densities ranging from 10^{20} m^{-3} up to 10^{22} m^{-3} [10,37]. The interstitial migration ability was strong at 350 °C [38] and easily accumulated in the (111) plane to increase the number density of the nucleation sites of dislocation loop [39]. This mechanism explains the orientation change in SLM 316L SS at 350 °C, as shown in GIXRD. Compared with CR 316L SS, its SLM counterpart had more dislocation loops but was smaller in size. This finding was contrary to Shang's [10] results possibly because the loop unfaulted and interacted to produce

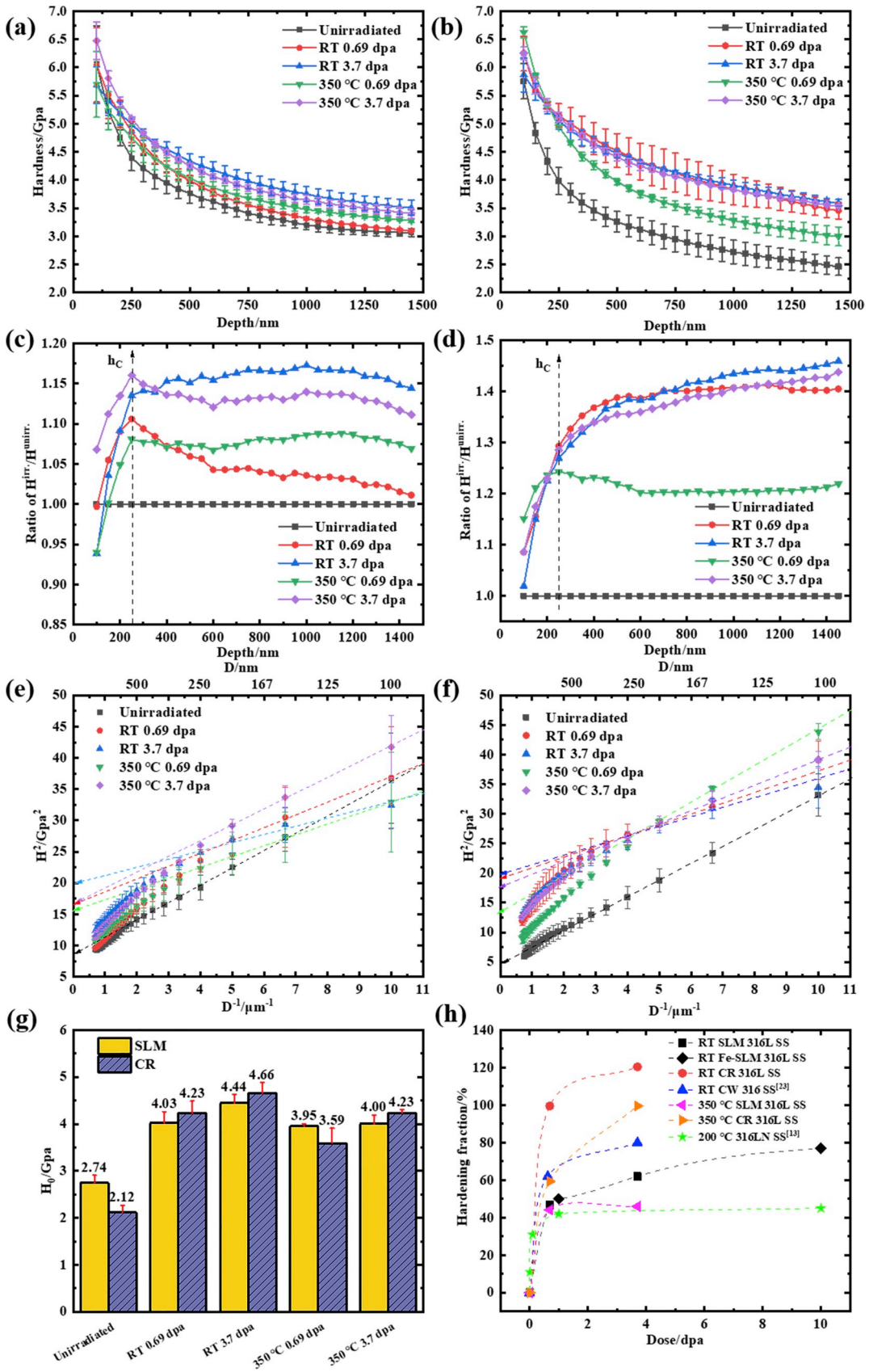

Fig. 6. Average hardness depending on indentation depth for (a) SLM and (b) CR 316L SS. Ratio of H^{irr}/H^{unirr} depending on indentation depth for (c) SLM and (d) CR 316L SS. H^2-1/D plots for (e) SLM and (f) CR 316L SS. (g) Comparison of the two steels' H_0 calculated via the Nix–Gao equation. (h) Comparison of the irradiation hardening of SLM and CR 316L SS (as a function of dose) with other literature results. (The results of our Fe ion irradiation SLM 316L SS have not been published. See Fig. S3 for details.)

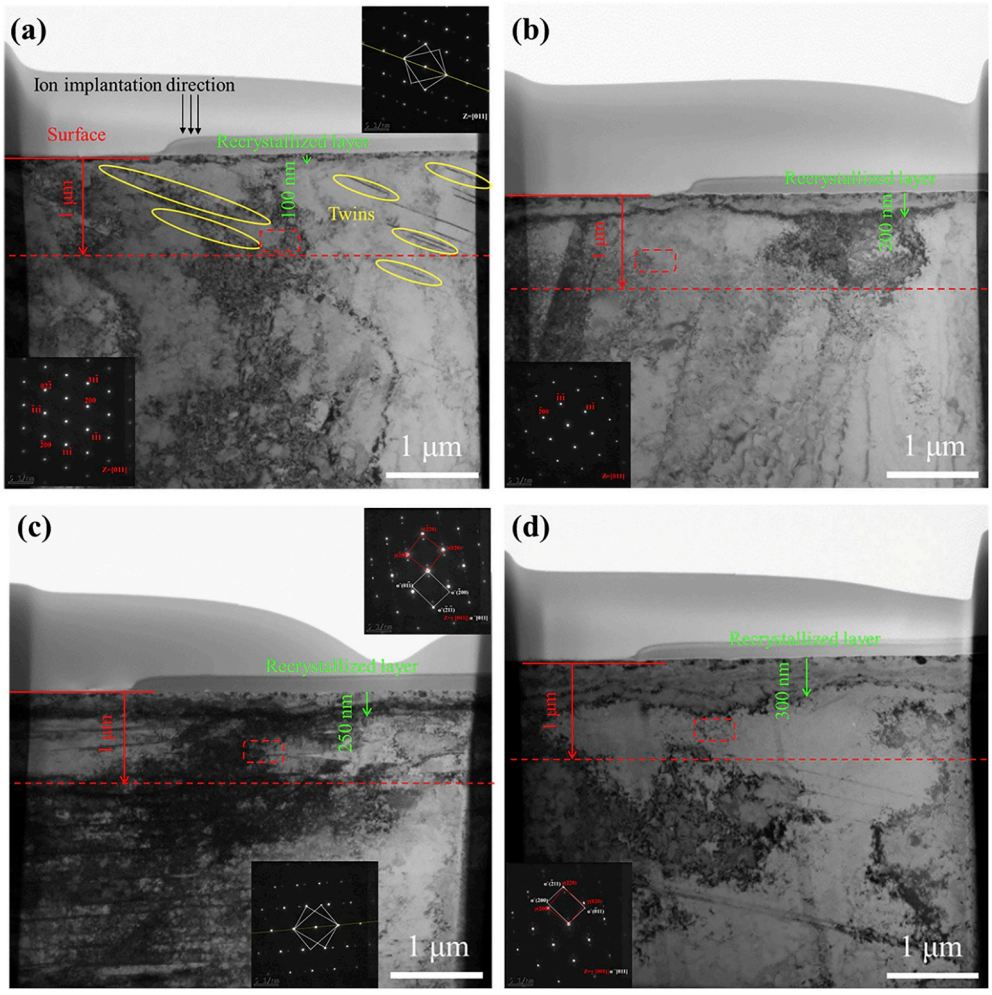

Fig. 7. Overall bright field (BF) TEM images of the two steels after irradiation at 3.7 dpa: SLM 316L SS at (a) RT and (b) 350 °C. CR 316L SS at (c) RT and (d) 350 °C. (The red rectangular areas represent the areas to be enlarged, whereas the yellow ellipse refer to twins.). (For interpretation of the references to colour in this figure legend, the reader is referred to the Web version of this article.)

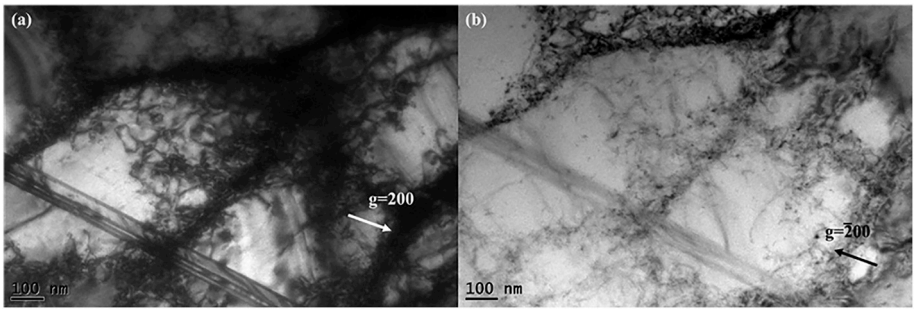

Fig. 8. TEM image of SLM 316L SS without irradiation. Micrographs were taken with beam direction B close to <1 1 0>. (a) g = 200, (b) g = −200.

network dislocations, which acted as nucleation sites for martensite [40] and resulted in reduced dislocation loops in CR 316L SS. However, a comparison of our results with those of Huang [23] (3.7×10^{22} m^{-3} for irradiated CW 316 SS without phase transition, 3.7 dpa, RT) reveals that the density of SLM 316L SS was less. This phenomenon was consistent with the explanation of the capturing effect of interface in SLM 316L SS.

3.6. STEM-EDS for Ar^+ irradiation

The cellular structures still clearly existed after irradiation to 3.7 dpa but became relatively diffused, as shown in Fig. 11. Song [11] attributed this phenomenon to recovery and recrystallization of the unstable sub-grains under the equivalent high temperature caused by irradiation. Further, Shang [10] confirmed that the SGBs are still stable even after irradiation to 5 dpa at 400 °C in spite of a relatively diffuse appearance. He proved that diffusion of the SGBs was due to irradiation-assisted dislocation climb. The element mapping result sill showed that Fe depleted, Cr, Ni and Mo segregated in SGBs after irradiation, which was similar to the result before irradiation. Fig. S1 showed that the mis-orientations of SGBs were <3°. Therefore, the boundary energy of SGBs is as low as low angle grain boundaries (LAGBs), making them stable under high temperature and irradiation. It is well known that the degree

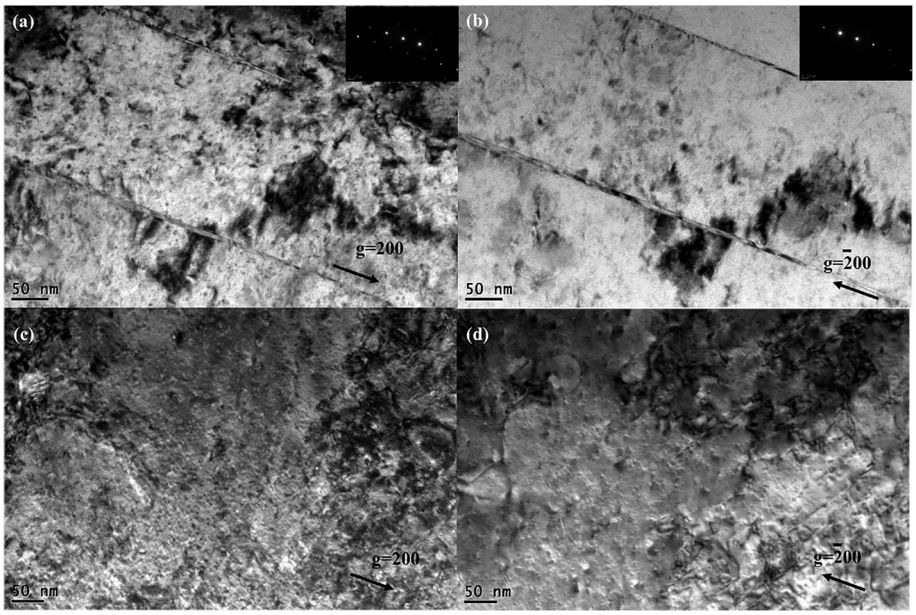

Fig. 9. TEM image of SLM 316L SS after irradiation. Micrographs were taken with beam direction B close to <110>. (a) g = 200 for RT, (b) g = −200 for RT; (c) g = 200 for 350 °C, (d) g = −200 for 350 °C.

of radiation-induced segregation (RIS) is proportional to the energy of grain boundary [41]. Thus, the RIS of SGBs is not obvious, which may due to the low grain boundary energy.

4. Discussion

4.1. Phase transition

Phase transition occurred in CR 316L SS at RT under 3.7 dpa irradiation. Notably, no phase transition occurred, but radiation-induced twins appeared in SLM 316L SS. This phenomenon could be explained by the twinning (TWIP)- and transformation (TRIP)-induced plasticity effects of the deformed austenitic steel in which strain-induced martensite and mechanical twins formed to accommodate additional strain caused by irradiation. The occurrence of these mechanisms was dependent on the stacking fault energy (SFE). TRIP was the main effect when SFE <20 mJ/m^2, whereas TWIP dominated when 15 < SFE <30 mJ/m^2 [42]. The factors affecting SFE were element composition, temperature, and grain size. Given that SLM and CR 316L SSs had similar elemental compositions and were performed under the same irradiation conditions, grain size was the dominant factor. Jun [43] proposed that an SFE of 15–20 μm austenite grains at 300 K was equal to 8–11 mJ/m^2. The average grain size of CR 316L SS was 17.25 μm; thus, TRIP was dominant. With the decrease in grain size, the fault energy increased gradually. The SGBs size of SLM 316L SS was only approximately 480 nm, which led to a high SFE. Therefore, TWIP was the main stress release mechanism that caused high austenite phase stability in SLM 316L SS.

4.2. Swelling

The TEM results showed that recrystallization occurred in the surface layer after irradiation, and some nanocrystals were formed. The increase in grain boundary volume led to a loose crystal structure, which likely contributed to surface swelling. However, no radiation swelling was observed in CR 316L SS at RT with a dose of 3.7 dpa, and recrystallization also occurred on its surface. Therefore, recrystallization was not the main cause of surface swelling. The formation of vacancy clusters and voids mainly contributed to swelling. In general, the temperature of irradiation-induced void formation is approximately 0.3–0.55 T_m. However, we observed swelling in SLM 316L SS without void formation at RT. Zhang [44] attributed this phenomenon to the interstitials expelled with the formation of vacancy-type defect. Given that no void formation was observed under TEM (likely due to insufficient irradiation dose), the dislocation loops can interact with the voids, we analyzed the swelling using following models:

The growth equation of void in general form is

$$dR/dt = (D_v C_v - D_i C_i - D_v C_v^{eq})\Omega/R, \quad (2)$$

where D_v, D_i and C_v, C_i are the diffusion coefficients and concentrations of vacancies and interstitials, respectively. C_v^{eq} is the vacancy equilibrium concentration. Ω is the atomic volume. In this equation, the growth rate of the void is determined by the rate of vacancies and interstitials flowing into the void. If we consider the sink strength, then the equation is transformed into [45].

$$dR/dt = \frac{\Omega D_i D_v}{2RK_i^v}\left[\left(1+\frac{4K_i^v K_0}{D_i D_v S_i S_v}\right)^{1/2} - 1\right](Z_v S_v - Z_i S_i), \quad (3)$$

where K_0 is the point defect generation rate, and $K_i^v$is the point defect recombination rate; S_i and S_v are the sink strength of interstitials and vacancies, respectively; Z_i and Z_v are the bias factors of the dislocation versus interstitials and vacancies, respectively. Dislocations, grain boundaries, and other defects can capture point defects. The grain boundary density of SLM 316L SS was 2.30–3.76 μm^{-1} (contains SGBs) in our work and 10 times that of its CR counterpart of 0.17 μm^{-1}. SLM 316L SS appeared to have strong sink strength S. However, grain boundaries with local misorientation greater than 5° were the effective traps for absorption point defects. The density of boundaries with more than 5° local misorientation in SLM 316L SS was approximately 0.20–0.30 μm^{-1} [8], which was almost equivalent to the boundary densities of CR 316L SS. The grain boundary trap strength S_{GB} of the two steels was therefore approximately equal with the dislocation bias as the main factor. Meric [8] proposed that the intermediate dislocation density in SLM 316L SS created an intermediate sink strength ratio. This ratio could lead to a higher dislocation sink bias in SLM 316L SS compared with that in its CR counterpart. Therefore, the swelling rate of SLM 316L SS was high. The results calculated using the above model deviate from the experimental results [24] because the influence of glissile dislocation loop was not considered. Meanwhile, the void

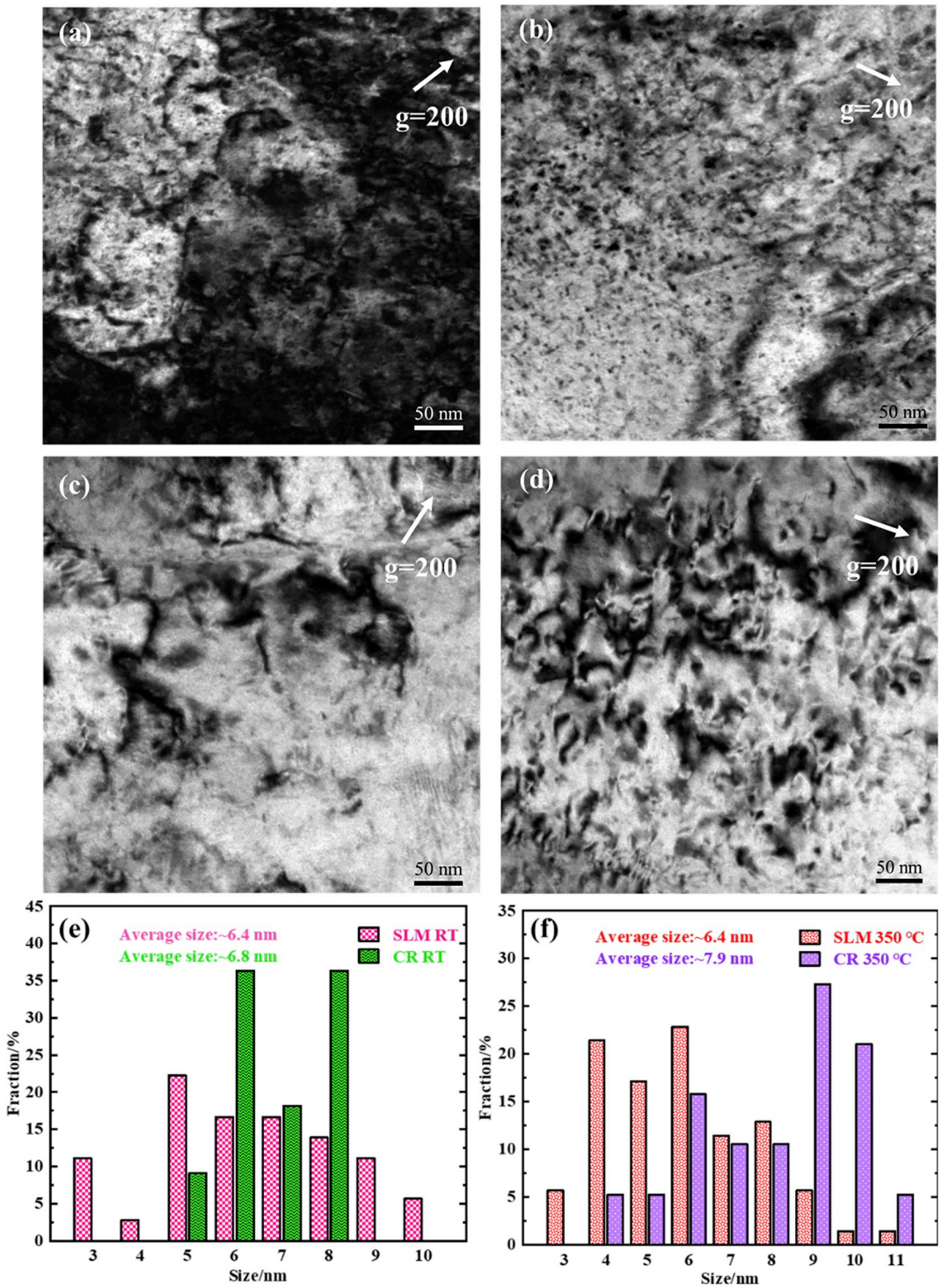

Fig. 10. BF TEM magnification images of the red rectangular areas in Fig. 6 belonging to the two steels after irradiation at 3.7 dpa: SLM 316L SS at (a) RT and (b) 350 °C. CR 316L SS at (c) RT and (d) 350 °C. The size distribution of dislocation loops in the damage peak region of the two steels after ion irradiation at (e) RT and (f) 350 °C. (For interpretation of the references to colour in this figure legend, the reader is referred to the Web version of this article.)

trapping of glissile dislocation loops could reduce the swelling rate [46]. Therefore, we considered the influence of the interstitial dislocation loops, where the dislocation loop is equivalent to the self-interstitial cluster. The form is changed into [47].

$$dS / dt = (D_v C_v Z_v^V - D_i C_i Z_i^V) k_v^2 - D_g C_g x_g k_g \pi R_v^2 \rho_v, \quad (4)$$

where K_v is the absorption strength of the void on point defect; D_g and C_g are the diffusion coefficient and concentration of self-interstitial cluster, respectively; k_g is the absorption strength of the sink to the interstitial cluster; x_g is the size of the interstitial cluster; and R_v and ρ_v are the average radius and density of the void, respectively. At RT, the swelling of SLM 316L SS was more evident than CR 316L SS. The void bias ($Z^V_v - Z^V_i$) was controlled by the size of the void. Given that voids were absent in the two 316L steels, we assumed that both steels had the same void bias, and the swelling rate was mainly affected by the right-hand side of Eq. (4). Dubinko [48] proved that high stacking energy

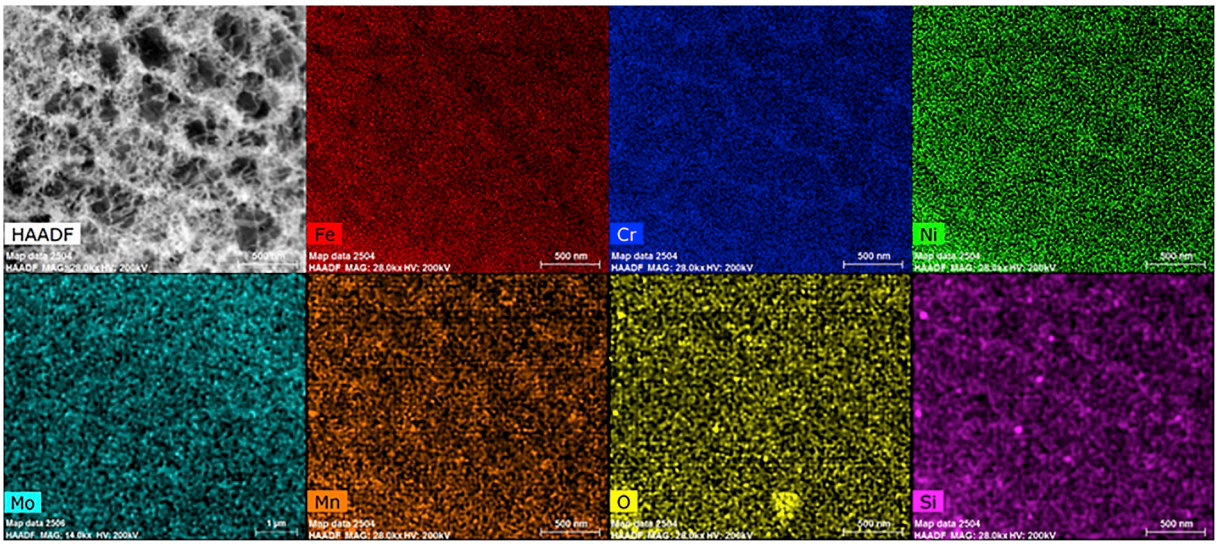

Fig. 11. Element mapping results of SLM 316L SS after Ar + irradiation to 3.7 dpa.

prevented slippage of dislocation loops and favored sessile perfect loops. Hence, D_g in SLM 316L SS was less than that in CR 316L SS due to the higher SFE in SLM 316L SS. Golubov [47] indicated that k_g was proportional to the dislocation density. The results showed that the dislocation density of as-fabricated AM 304 SS was one-fifth that of conventional 304 SS and strained to −11% [49]. The deformation of CR 316L SS in our study was 15%, indicating a higher dislocation density and larger k_g compared with those of SLM 316L SS. In addition, the annihilated concentration C_g was inversely proportional to the remaining dislocation loop density. Hence, SLM 316L SS obtained a high swelling rate at RT due to the small values of D_g, k_g, and C_g. However, at 350 °C, the difference in the diffusion coefficient D_g reduced due to the decrease in the difference in SFE. As a result, the difference of swelling between the two steels also decreased.

There are other factors in SLM 316L SS that affect the swelling. Meric [8] indicated that the interface between nanoclusions and matrix in AM 316L SS would capture voids. However, the local swelling inhibition by nanoclusions is not expected to counterbalance the overall swelling due to the limited number density. Heald [50] proposed that the presence of vacancy loops reduced the swelling rates in metals due to the reduction of effective displacement damage rate. Kiritani [32] also found the suppression of the formation of irradiated induced dislocation loops by vacancy loops in Al. It can be inferred that the pre-existing vacancy dislocation loops in SLM 316L SS can inhibit swelling. But it still couldn't counterbalance the overall swelling.

The correlation between swelling and RIS in SLM 316L SS needs to be investigated. Allen [51] indicated that RIS could affect swelling by decreasing the vacancy flux to the void. Due to the lower diffusivity of Ni via the vacancy flux relative to Cr, in all austenitic Fe–Cr–Ni alloys, Ni enriches and Cr depletes at void surfaces during irradiation. The local composition change reduces the subsequent vacancy flux to the voids, increasing the bulk point defect recombination rate, reducing the bulk vacancy concentration, which further reduces swelling. RIS profiles show similar trends at void surfaces as they do at grain boundaries Thus the larger RIS degree (radio of Ni enrichment compared to Cr depletion) at grain boundaries in Fe–Cr–Ni alloys, the smaller swelling would be. There was no RIS and the radio of Ni enrichment compared to Cr depletion was low at the SGBs in SLM 316L SS after irradiation at RT. The nucleation and growth of the void could not be suppressed by elements segregation, so the swelling of SLM 316L SS would not be inhibited at RT.

In summary, dislocation bias and D_g are the main factors affecting the swelling of SLM 316L SS.

4.3. Hardening

The effect of element segregation at SGBs on the mechanical properties of SLM 316L SS was considered. Due to the stabilizing effect of the solute acts to pin the SGBs (solute/SGB interaction), the hardness of SLM 316L SS increases effectively. However, the segregation at SGBs of SLM 316L SS was not changed obviously by irradiation at RT. Therefore, the micro change of element composition at the SGBs is not the main reason for the change in hardness after irradiation at RT. At elevated temperatures or under irradiation, residual stress in SLM 316L SS will be released due to the Porte-vin–Le Chatelier effect [15] and accelerated atomic diffusion. The material should appear lower effective yield limit [15] and softened at 350 °C and after irradiation. Thus, pre-existing stresses and strain did not primarily affect radiation hardening. Formation of radiation-induced defects may dominate radiation hardening.

Given that the yield stress of materials is proportional to hardness, the contribution of irradiation defects on the hardening phenomenon could be interpreted by the dispersed barrier hardening (DBH) model [52], as follows:

$$\Delta\sigma_y = \alpha M \mu b \sqrt{Nd}, \tag{5}$$

where $\Delta\sigma_y$ is the increase in yield strength; α is the defect barrier strength; M is the Taylor factor (3.06 for equiaxed BCC and FCC structure metals); μ is the shear modulus; b is the module of Burgers vector; and N and d are the density and diameter of the defect cluster, respectively. For 316L SS, M, μ, and b are constants; and α, N, and d are different in SLM and CR. If only the influence of the dislocation loop is considered, then the yield strength increment of SLM 316L at RT is nearly 2.9 times that of CR 316L SS. However, the hardening of CR is higher than that of SLM because the factors causing hardening in the material are located not only the dislocation loop but also in the precipitated phase, such as martensite. Studies have shown that the α of the dislocation loop is 0.25–0.5, whereas α of the precipitated phase is approximately 0.3–1 [31,53]. Given that CR 316L SS at 3.7 dpa had approximately 55% martensite, the hardening degree was higher than that of SLM 316L SS. At RT, SLM 316L SS produced some twins, which increased hardening. Therefore, hardening at RT was greater than that at 350 °C even in the case of a smaller loop density.

5. Conclusions

In this study, the degree of phase transition, swelling, and hardening between irradiated SLM and CR 316L SSs were compared at RT and 350

°C with 5 MeV Xe^{23+} ions. GIXRD, AFM, nanoindentation, and TEM were used for the comparison. The ion doses were calculated at 0.69 and 3.7 dpa. Compared with CR 316L SS, SLM 316L SS exhibited higher phase stability due to the fine-grained strengthening effect. The swelling degree of SLM 316L SS at RT was higher than that of CR 316L SS because of the differences in the dislocation density, diffusion coefficient (D_g), and concentration (C_g) of interstitial clusters, such as loops between the two steels. The swelling degree of the two steels was almost the same at 350 °C due to the decrease in differences in dislocation bias and D_g. The hardening of CR 316L SS was stronger than that of SLM 316L SS with a lower dislocation loop density at RT and 350 °C. The formation of radiation-induced martensite caused the hardening of CR 316L SS.

The radiation swelling of austenitic steels is a huge problem during nuclear reactor operation; thus, the radiation swelling properties of SLM 316L SS must be further adjusted. In future studies, aging treatment on SLM 316L SS may be an effective technique to improve the ratio of the large-angle grain boundary (≥5°) and change the boundary distribution, which is expected to further improve the radiation swelling resistance of AM 316L SS.

Declaration of competing interest

We declare that we have no known competing financial interests or personal relationships that could have appeared to influence the work reported in this paper.

Acknowledgement

The authors would like to acknowledge support from the National Natural Science Foundation of China [Grant No. 11705087], the Natural Science Foundation of Jiangsu Province [Grant No. BK20170776], the Postgraduate Research & Practice Innovation Program of Jiangsu Province [Grant No. SJCX18_0109], and the Foundation of Graduate Innovation Center in [Grant No. kfjj20190604]. We further thank to the 320-kV platform at the Institute of Modern Physics, CAS for the support of irradiation experiment. Thanks to the Suzhou Institute of Nano-Tech and Nano-Bionics, CAS for the support of Nanoindentation tests. We futher thank the help of Aiqun Xu from Southeast University for TEM experiments.

Appendix A. Supplementary data

Supplementary data to this article can be found online at https://doi.org/10.1016/j.vacuum.2020.109183.

References

[1] C. Gao, X. Chen, C. Su, X. Chen, Location dependence of microstructure and mechanical properties on wire arc additively manufactured nuclear grade steel, Vacuum 168 (2019), 108818.
[2] X. Zhao, D. Gu, C. Ma, L. Xi, H. Zhang, Microstructure characteristics and its formation mechanism of selective laser melting SiC reinforced Al-based composites, Vacuum 160 (2019) 189–196.
[3] E. Liverani, S. Toschi, L. Ceschini, A. Fortunato, Effect of selective laser melting (SLM) process parameters on microstructure and mechanical properties of 316L austenitic stainless steel, J. Mater. Process. Technol. 249 (2017) 255–263.
[4] Q. Chao, V. Cruz, S. Thomas, N. Birbilis, P. Collins, A. Taylor, P.D. Hodgson, D. Fabijanic, On the enhanced corrosion resistance of a selective laser melted austenitic stainless steel, Scr. Mater. 141 (2017) 94–98.
[5] S. Wang, J. Li, Y. Cao, B. Gao, Q. Mao, Y. Li, Thermal stability and tensile property of 316L stainless steel with heterogeneous lamella structure, Vacuum 152 (2018) 261–264.
[6] Y. Zhong, L.-E. Rännar, S. Wikman, A. Koptyug, L. Liu, D. Cui, Z. Shen, Additive manufacturing of ITER first wall panel parts by two approaches: selective laser melting and electron beam melting, Fusion Eng. Des. 116 (2017) 24–33.
[7] B. Huang, Y. Zhai, S. Liu, X. Mao, Microstructure anisotropy and its effect on mechanical properties of reduced activation ferritic/martensitic steel fabricated by selective laser melting, J. Nucl. Mater. 500 (2018) 33–41.
[8] G.M. de Bellefon, K. Bertsch, M. Chancey, Y. Wang, D. Thoma, Influence of solidification structures on radiation-induced swelling in an additively-manufactured austenitic stainless steel, J. Nucl. Mater. 523 (2019), 291e298.
[9] J.A. Evans, S.A. Anderson, E.J. Faierson, D. Perez-Nunez, S.M. McDeavitt, Anisotropic radiation-induced changes in type 316L stainless steel rods built by laser additive manufacturing, Nucl. Technol. 205 (4) (2019) 563–581.
[10] Z. Shang, C. Fan, S. Xue, J. Ding, J. Li, T. Voisin, Y. Wang, H. Wang, X. Zhang, Response of solidification cellular structures in additively manufactured 316 stainless steel to heavy ion irradiation: an in situ study, Materials Research Letters 7 (7) (2019) 290–297.
[11] M. Song, M. Wang, X. Lou, R.B. Rebak, G.S. Was, Radiation damage and irradiation-assisted stress corrosion cracking of additively manufactured 316L stainless steels, J. Nucl. Mater. 513 (2019) 33–44.
[12] X. Sun, F. Chen, H. Huang, J. Lin, X. Tang, Effects of interfaces on the helium bubble formation and radiation hardening of an austenitic stainless steel achieved by additive manufacturing, Appl. Surf. Sci. 467 (2019) 1134–1139.
[13] J. Hunn, E. Lee, T. Byun, L. Mansur, Helium and hydrogen induced hardening in 316LN stainless steel, J. Nucl. Mater. 282 (2–3) (2000) 131–136.
[14] L. Liu, Q. Ding, Y. Zhong, J. Zou, J. Wu, Y.-L. Chiu, J. Li, Z. Zhang, Q. Yu, Z. Shen, Dislocation network in additive manufactured steel breaks strength–ductility trade-off, Mater. Today 21 (4) (2018) 354–361.
[15] A.J. Birnbaum, J.C. Steuben, E.J. Barrick, A.P. Iliopoulos, J.G. Michopoulos, Intrinsic strain aging, Σ3 boundaries, and origins of cellular substructure in additively manufactured 316L, Additive Manufacturing 29 (2019), 100784.
[16] A.K. De, D.C. Murdock, M.C. Mataya, J.G. Speer, D.K. Matlock, Quantitative measurement of deformation-induced martensite in 304 stainless steel by X-ray diffraction, Scr. Mater. 50 (12) (2004) 1445–1449.
[17] N.K. Kumar, C. Li, K. Leonard, H. Bei, S. Zinkle, Microstructural stability and mechanical behavior of FeNiMnCr high entropy alloy under ion irradiation, Acta Mater. 113 (2016) 230–244.
[18] S. Kajiwara, Roles of dislocations and grain boundaries in martensite nucleation, Metall. Mater. Trans. A 17 (10) (1986) 1693–1702.
[19] M.I. Mendelev, Y. Mishin, Molecular dynamics study of self-diffusion in bcc Fe, Phys. Rev. B 80 (14) (2009), 144111.
[20] E. Lee, Y. Lee, W. Oliver, L. Mansur, Hardness measurements of Ar+-beam treated polyimide by depth-sensing ultra low load indentation, J. Mater. Res. 8 (2) (1993) 377–387.
[21] W.D. Nix, H. Gao, Indentation size effects in crystalline materials: a law for strain gradient plasticity, J. Mech. Phys. Solids 46 (3) (1998) 411–425.
[22] R. Kasada, Y. Takayama, K. Yabuuchi, A. Kimura, A new approach to evaluate irradiation hardening of ion-irradiated ferritic alloys by nano-indentation techniques, Fusion Eng. Des. 86 (9–11) (2011) 2658–2661.
[23] H. Huang, J. Li, D. Li, R. Liu, G. Lei, Q. Huang, L. Yan, TEM, XRD and nanoindentation characterization of Xenon ion irradiation damage in austenitic stainless steels, J. Nucl. Mater. 454 (1–3) (2014) 168–172.
[24] U. Theis, H. Wollenberger, Mobile interstitials produced by neutron irradiation in copper and aluminium, J. Nucl. Mater. 88 (1) (1980) 121–130.
[25] T. Byun, On the stress dependence of partial dislocation separation and deformation microstructure in austenitic stainless steels, Acta Mater. 51 (11) (2003) 3063–3071.
[26] X. Zhang, K. Hattar, Y. Chen, L. Shao, J. Li, C. Sun, K. Yu, N. Li, M.L. Taheri, H. Wang, Radiation damage in nanostructured materials, Prog. Mater. Sci. 96 (2018), 217-321.
[27] J.E. Jung, J. Park, J.-S. Kim, J.B. Jeon, S.K. Kim, Y.W. Chang, Temperature effect on twin formation kinetics and deformation behavior of Fe-18Mn-0.6 C TWIP steel, Met. Mater. Int. 20 (1) (2014) 27–34.
[28] W.V. Vaidya, K. Ehrlich, Radiation-induced recrystallization, its cause and consequences in heavy-ion irradiated 20% cold-drawn steels of type 1.4970, J. Nucl. Mater. 113 (2–3) (1983) 149–162.
[29] Y. Shen, X. Li, X. Sun, Y. Wang, L. Zuo, Twinning and martensite in a 304 austenitic stainless steel, Mater. Sci. Eng. A 552 (2012) 514–522.
[30] Y. Chen, H. Wang, M.A. Kirk, M. Li, J. Wang, X. Zhang, Radiation induced detwinning in nanotwinned Cu, Scr. Mater. 130 (2017) 37–41.
[31] K.S. Mao, C. Sun, Y. Huang, C.-H. Shiau, F.A. Garner, P.D. Freyer, J.P. Wharry, Grain orientation dependence of nanoindentation and deformation-induced martensitic phase transformation in neutron irradiated AISI 304L stainless steel, Materialia 5 (2019), 100208.
[32] M. Kiritani, N. Yoshida, H. Takata, Interstitial clusters in electron irradiated aluminum, J. Phys. Soc. Jpn. 36 (3) (1974) 720–729.
[33] A. Rowcliffe, R. Nicholson, Quenching defects and precipitation in a phosphorus-containing austenitic stainless steel, Acta Metall. 20 (1) (1972) 143–155.
[34] Y.Y. Kaplanskii, A. Zaitsev, E. Levashov, P. Loginov, Z.A. Sentyurina, NiAl based alloy produced by HIP and SLM of pre-alloyed spherical powders. Evolution of the structure and mechanical behavior at high temperatures, Mater. Sci. Eng. A 717 (2018) 48–59.
[35] M.L. Jenkins, M.A. Kirk, Characterisation of Radiation Damage by Transmission Electron Microscopy, CRC Press, 2000.
[36] C. English, B. Eyre, J. Summers, Influence of irradiation temperature on self-ion damage in copper, Philos. Mag.: A Journal of Theoretical Experimental and Applied Physics 34 (4) (1976) 603–614.
[37] C. Bailat, F. Gröschel, M. Victoria, Deformation modes of proton and neutron irradiated stainless steels, J. Nucl. Mater. 276 (1–3) (2000) 283–288.
[38] B. Wirth, G. Odette, D. Maroudas, G. Lucas, Energetics of formation and migration of self-interstitials and self-interstitial clusters in α-iron, J. Nucl. Mater. 244 (3) (1997) 185–194.
[39] T.D. De La Rubia, M. Guinan, New mechanism of defect production in metals: a molecular-dynamics study of interstitial-dislocation-loop formation in high-energy displacement cascades, Phys. Rev. Lett. 66 (21) (1991) 2766.

[40] E. Lee, N. Packan, L. Mansur, Effects of pulsed dual-ion irradiation on phase transformations and microstructure in Ti-modified austenitic alloy, J. Nucl. Mater. 117 (1983) 123–133.
[41] N. Sakaguchi, M. Endo, S. Watanabe, H. Kinoshita, S. Yamashita, H. Kokawa, Radiation-induced segregation and corrosion behavior on Σ3 coincidence site lattice and random grain boundaries in proton-irradiated type-316L austenitic stainless steel, J. Nucl. Mater. 434 (1–3) (2013) 65–71.
[42] E.I. Galindo-Nava, P. Rivera-Díaz-del-Castillo, Understanding martensite and twin formation in austenitic steels: a model describing TRIP and TWIP effects, Acta Mater. 128 (2017) 120–134.
[43] J.-H. Jun, C.-S. Choi, Variation of stacking fault energy with austenite grain size and its effect on the MS temperature of γ→ ε martensitic transformation in Fe–Mn alloy, Mater. Sci. Eng. A 257 (2) (1998) 353–356.
[44] S. Zhang, D. Li, H. Chen, G. Lei, H. Huang, W. Zhang, C. Wang, L. Yan, D. Fu, M. Tang, Ion irradiation-induced swelling and hardening effect of Hastelloy Náalloy, J. Nucl. Mater. 489 (2017) 180–186.
[45] L. Mansur, Theory and experimental background on dimensional changes in irradiated alloys, J. Nucl. Mater. 216 (1994) 97–123.
[46] S. Jin, B. Mo, W. Zhang, T. Zhang, Y. Li, L. Guo, X. Cao, B. Wang, Towards understanding the evolution of dislocation loops and their interaction with vacancies in Fe9Cr alloy during the irradiation swelling incubation period, Materialia 5 (2019), 100241.
[47] S. Golubov, B. Singh, H. Trinkaus, Defect accumulation in fcc and bcc metals and alloys under cascade damage conditions–Towards a generalisation of the production bias model, J. Nucl. Mater. 276 (1–3) (2000) 78–89.
[48] V. Dubinko, Impact of glissile interstitial loop production in cascades on void ordering and swelling saturation under irradiation, Nucl. Instrum. Methods Phys. Res. Sect. B Beam Interact. Mater. Atoms 102 (1–4) (1995) 125–131.
[49] D. Brown, D. Adams, L. Balogh, J. Carpenter, B. Clausen, G. King, B. Reedlunn, T. Palmer, M. Maguire, S. Vogel, In situ neutron diffraction study of the influence of microstructure on the mechanical response of additively manufactured 304L stainless steel, Metall. Mater. Trans. A 48 (12) (2017) 6055–6069.
[50] P. Heald, M. Speight, The influence of cascade damage on irradiation creep and swelling, J. Nucl. Mater. 64 (1–2) (1977) 139–144.
[51] T. Allen, J. Cole, J. Gan, G. Was, R. Dropek, E. Kenik, Swelling and radiation-induced segregation in austentic alloys, J. Nucl. Mater. 342 (1–3) (2005) 90–100.
[52] M. Lambrecht, E. Meslin, L. Malerba, M. Hernández-Mayoral, F. Bergner, P. Pareige, B. Radiguet, A. Almazouzi, On the correlation between irradiation-induced microstructural features and the hardening of reactor pressure vessel steels, J. Nucl. Mater. 406 (1) (2010) 84–89.
[53] S.J. Zinkle, Y. Matsukawa, Observation and analysis of defect cluster production and interactions with dislocations, J. Nucl. Mater. 329 (2004) 88–96.